



HAL
open science

Quantitative in situ visualization of thermal effects on the formation of gold nanocrystals in solution

Abdelali Khelfa, Jaysen Nelayah, Hakim Amara, Guillaume Wang, Christian Ricolleau, Damien Alloyeau

► **To cite this version:**

Abdelali Khelfa, Jaysen Nelayah, Hakim Amara, Guillaume Wang, Christian Ricolleau, et al.. Quantitative in situ visualization of thermal effects on the formation of gold nanocrystals in solution. *Advanced Materials*, 2021, 33 (38), pp.2102514. 10.1002/adma.202102514 . hal-03414114

HAL Id: hal-03414114

<https://hal.science/hal-03414114>

Submitted on 4 Nov 2021

HAL is a multi-disciplinary open access archive for the deposit and dissemination of scientific research documents, whether they are published or not. The documents may come from teaching and research institutions in France or abroad, or from public or private research centers.

L'archive ouverte pluridisciplinaire **HAL**, est destinée au dépôt et à la diffusion de documents scientifiques de niveau recherche, publiés ou non, émanant des établissements d'enseignement et de recherche français ou étrangers, des laboratoires publics ou privés.

Quantitative *in situ* visualization of thermal effects on the formation of gold nanocrystals in solution

Abdelali Khelfa,^a Jaysen Nelayah,^a Hakim Amara,^{a,b} Guillaume Wang,^a Christian Ricolleau,^a
Damien Alloyeau^{a,*}

^aLaboratoire Matériaux et Phénomènes Quantiques, Université de Paris - CNRS, Paris, France

^bLaboratoire d'Études des Microstructures, ONERA - CNRS - Université Paris Saclay, Chatillon,
France

*Corresponding author:

Damien Alloyeau, Tel: +33 1 57 27 69 83, E-mail: damien.alloyeau@univ-paris-diderot.fr

Keywords: gold nanoparticles, liquid-phase synthesis, *in situ* TEM, temperature, kinetics, thermodynamics, LSW theory

Abstract

Understanding temperature effects in nanochemistry requires real time *in situ* measurements because this key parameter of wet-chemical synthesis simultaneously influences the kinetics of chemical reactions and the thermodynamic equilibrium of nanomaterials in solution. Here, we exploit temperature-controlled liquid cell transmission electron microscopy to directly image the radiolysis-driven formation of gold nanoparticles between 25 °C and 85 °C and provide a deeper understanding of the atomic-scale processes determining the size and shape of gold colloids. By quantitatively comparing the nucleation and growth rates of colloidal assemblies with classical models for nanocrystal formation, we show that the increase of molecular diffusion and nanoparticle solubility governs the drastic changes in the formation dynamics of nanostructures in

solution with temperature. In contraction with the common view of coarsening processes in solution, we also demonstrate that the dissolution of nanoparticles and thus the Ostwald ripening are not only driven by size effects. Furthermore, visualizing thermal effects on faceting processes at the single nanoparticle level reveals how the competition between the growth speed and the surface diffusion dictates the final shape of nanocrystals.

1. Introduction

Temperature is a crucial parameter in the liquid-phase synthesis of metal nanoparticles (NPs) that directly impacts all the atomic-scale processes that drive the size dispersion of colloidal assemblies and the shape of nanostructures, including the reaction and diffusion of metal precursors in solution, the nucleation of clusters, the adsorption, desorption and diffusion of metal atoms on nanocrystals, the Ostwald ripening and the coalescence mechanisms. ^[1] Therefore, many synthesis strategies based on temperature control in classical or high boiling points solvents have been developed to tune the size, shape and crystallinity of nanostructures. ^[2] However, as the temperature concomitantly affects the kinetic and thermodynamic of nucleation and growth processes, the full understanding of thermal effects requires time-resolved *in situ* analyses. On the one hand, the formation of metal NPs can be studied in synthesis environments with variable composition and temperature using global analysis techniques, such as X-ray scattering methods or/and UV Visible spectroscopy, that allow real-time averaged measurements of the size, shape, density and volume fraction of nano-objects. ^[3] Thermal effects on the nucleation and growth kinetics can then be investigated in large volume of solution and compared with the classical theoretical models for nanocrystal formation. ^[1b, 4] However, given the necessity to make hypotheses to retrieve the structural information, these *in situ* approaches provide an indirect and incomplete overview of the

NP dynamics in solution, particularly when size and shape dispersity are important. On the other hand, liquid-cell transmission electron microscopy (LCTEM) has become a cutting edge method to take a direct look at NP synthesis with tunable spatial resolutions.^[5] Interestingly, the dynamics of colloidal assemblies composed of several hundred nano-objects can be monitored to extract statistical information on the nucleation and growth processes^[6] and the chemical reactions can also be observed at the single NP level to provide *in situ* insights into the atomic scale mechanisms driving NP shape.^[7] However, as the use of LCTEM with temperature control is very recent,^[8] the direct observations of thermal effects on the formation processes of nanomaterials are still in their infancy.

Here, we exploit temperature-controlled LCTEM to study thermal effects on the radiolysis-driven formation of gold nanocrystals in water between 25 °C and 85 °C. The drastic impacts of temperature on the nucleation and growth rates of nanostructures are quantitatively explained in the framework of the classical theories and reveal the key roles of molecular diffusion and NP solubility on the behavior of colloidal assemblies. Moreover, visualizing the coarsening and surface diffusion processes level at different temperatures with high resolution provides a mechanistic understanding of nanocrystal growth that goes beyond the classical models.

2. Results and discussions

2.1. Temperature effects on the nucleation and growth processes: when molecular diffusion and solution solubility rule the dynamics of colloids

When aqueous solutions of metal precursors are studied by LCTEM, the radiolysis of water produces reducing and oxidizing species, including aqueous electrons and hydrogen radicals that reduce the metal precursors and drive the nucleation and growth of metal NPs at the interface between the SiN membrane and the solution. As the concentration of reducing agents increases

with the electron dose rate (\dot{d}),^[9] the control of the nucleation and growth rates with this finely tunable parameter has been deeply exploited to investigate kinetic effects on the growth of metal NPs,^[10] including gold NPs.^[6c, 11] Thus, studying thermal effects on NPs formation requires comparing *in situ* TEM videos acquired with the same electron dose rate. **Figure 1** shows the growth of gold NPs in an aqueous solution of chloroauric acid (1 mM) at 25 °C, 50 °C and 85 °C in low electron dose rate ($\dot{d} = 3.4 \text{ electrons.nm}^{-2}.\text{s}^{-1}$) and low magnification conditions that offer a large field of view ($44.4 \mu\text{m}^2$). See experimental section for details. Remarkably, the formation dynamics of NPs varies greatly in this temperature range. At 25 °C, a dense assembly of small NPs (about 90 nm in size) is formed over 75 s (Figure 1a). At 50 °C, the colloidal assembly is less dense and similar sizes are reached after only 30 s (Figure 1b). At 85 °C, only a few tens of NPs are formed with size ranging from 300 nm to 2 μm after 75s (Figure 1c). In line with previous works on the growth of NPs in low dose conditions,^[6c, 10a] two populations of objects are formed during these three growth experiments: highly contrasted small 3D NPs and large 2D nanostructures with triangular or hexagonal shapes and a lower contrast (Figure 1 and S1).

Automated video processing based on interface-tracking algorithms was exploited to quantify thermal effects on the behavior of colloidal assemblies.^[12] **Figure 2a** shows the evolution of the number of detected NPs (N) as a function of time (t). In agreement with the visual inspection of *in situ* videos, automated particle tracking shows that N strongly drops with temperature (Figure 2a), from 880 NPs at 25 °C to 280 and 30 NPs at 50 °C and 85 °C, respectively at the end of the nucleation phase (i.e. when N reaches its maximum). However, the density of NPs is more affected by the duration of nucleation phase rather than a change in the nucleation rate. Indeed, the nucleation period lasts 28 s at 25 °C, 8 s at 50 °C and 2.6 s at 85 °C, where 93% of the NPs detected over the experiment appear on the very first image of the video. The average nucleation rates

calculated over the whole nucleation period (30 NPs/s and 35 NPs/s) and the instantaneous nucleation rate calculated at the early stage of the experiments are rather similar at 25 °C and 50 °C. Given the time resolution of the observations, such measurements cannot be made in a relevant manner on the very short nucleation burst observed at 85 °C.

According to the classical nucleation theory, ^[1b, 3e, 4a] the nucleation rate of gold NPs at the solution/substrate interface is given by:

$$\frac{dN}{dt} = A \exp\left(-\frac{\emptyset \Delta G_{hom}}{k_b T}\right) = A \exp\left(-\frac{16 \emptyset \pi \gamma^3 V_m^2}{3 k_b^3 T^3 N_a (\ln S)^2}\right) \quad (1)$$

where ΔG_{hom} is the free energy barrier to homogenous nucleation in solution, \emptyset is a reducing factor of this energy barrier due to presence of interfaces and A , k_b , N_a , T , γ , S and V_m are a pre-exponential factor, the Boltzmann constant, the Avogadro's number, the temperature, the surface energy of gold nanocrystals, the supersaturation ratio and the molar volume of the solution, respectively. From this Arrhenius plot drawn in **figure 3a** with $\emptyset = 0.5$ and $\gamma = 0.5 \text{ J. m}^{-2}$,^[3b, 13] we see that the nucleation rate is expected to increase with T and S . Therefore, the shortening of the nucleation period with temperature is necessarily due to a faster decrease of S during the high-temperature experiments. S corresponds to the ratio between the concentration of gold atoms in the irradiated area (C_{Au}) and the equilibrium solubility of the solution (C_∞). The dynamics of C_{Au} can be evaluated by measuring the total volume of gold NPs (V_{tot}) over time corresponding to the consumption of gold precursors in the solution due to growth processes. V_{tot} was calculated from the measurements of the surface area of NPs on the images (Figure 2b), by considering that all the NPs are spherical, apart from the four large 2D NPs observed at 85 °C. In a previous study,^[6c] we demonstrated that on average the volume of those 2D NPs grows at the same speed than the 3D NPs. Therefore the contribution of these 2D NPs was taken into account by adding four spherical NPs of average

volume to the total volume of gold crystals. Interestingly, although NP density reduces rapidly with temperature, the consumption rate of gold precursors in the NPs increases with temperature (Figure 2b) and we can estimate that C_{Au} decreases almost twice as fast at 85 °C as at 25 °C. However, we note that the total volume of gold NPs at the end of the nucleation phase is significantly higher at 25 °C ($0.16 \mu\text{m}^3$), than at 50 °C ($5.7 \cdot 10^{-2} \mu\text{m}^3$) and 85 °C ($4.1 \cdot 10^{-2} \mu\text{m}^3$). This latter result highlights that the decrease of C_{Au} is not the only parameter that influences S . Indeed, in most colloidal solutions, including gold NPs in water,^[14] C_∞ increases with increasing temperature. Therefore, although C_{Au} in the liquid-cell is the same at the very beginning of the experiments, S is still lower at 85 °C than at 25 °C, which combined with the faster dynamics of the nanocrystal growth, considerably shorten the nucleation phase.

The quantitative study of the growth processes allows further evaluation of the effect of temperature on C_∞ , a key parameter to understand dynamics of colloids in solution. We measured the evolution of the mean radius of NPs (\bar{r}) over time (**Figure S2a**). As seen on the logarithmic relationship between \bar{r} and t (Figure 2c), similar growth trajectories are observed at 25 °C, 50 °C and 85 °C with \bar{r} varying as $t^{1/3}$. Such growth kinetics are in line with the diffusion-limited growth model described in the Lifshitz–Slyozov–Wagner (LSW) theory,^[1b, 4b, 4c] according to which:

$$\bar{r}^3 = Kt \quad (2)$$

Obviously, the growth of NPs considerably speeds-up with temperature, but this only increases the growth rate constant K while the power law exponent stays unchanged, which in the framework of the LSW theory means that diffusion remains the limiting factor of the growth processes in this temperature range. From the linear fits of the curves $\bar{r}^3 = Kt$ (Figure S2b-d), we measured that K increases from $1.3 \cdot 10^3 \text{ nm}^3 \cdot \text{s}^{-1}$ at 25 °C to $4.5 \cdot 10^3 \text{ nm}^3 \cdot \text{s}^{-1}$ and $7.9 \cdot 10^4 \text{ nm}^3 \cdot \text{s}^{-1}$ at 50 °C and 85 °C,

respectively. The activation energy for NP growth deduced from linear fit of the Arrhenius plot of K (Figure 2d) is $61 \text{ kJ}\cdot\text{mol}^{-1}$ corresponding to 0.63 eV/atom . As a comparison, Abécassis et al. found a similar energy barrier by studying the temperature-dependent kinetics of gold-NP growth driven by the reduction of AuCl_3 by BH_4^- in toluene by combining real-time SAXS and XANES analyses.^[3g]

The growth of gold nanocrystals in the liquid-cell is mainly driven by monomer adsorption. The reservoir of metal precursors is the same at the beginning of all experiments (see materials and methods) and by considering a liquid thickness of 500 nm , we can calculate that there are $1.3 \cdot 10^7$ molecules of HAuCl_4 in the observation area before irradiation. As the number of gold atoms within the NPs exceed this amount of gold precursors after only one second of growth (Figure 2b), we know that gold supply mostly comes from external area, making the diffusion of gold precursors to the irradiated area a limiting factor for the growth of NPs. Therefore, the increase of molecular diffusion with temperature greatly contributes to the boost of gold reduction observed at high temperature. The effect of atomic diffusion is taken into account in the LSW model, ^[1b, 4b, 4c] through the expression of the growth rate constant:

$$K = \frac{8\gamma DV_m^2 C_\infty}{9RT} \quad (3)$$

with V_m the molar volume, R the universal gas constant. D corresponds to the diffusion coefficient given by the Stoke-Einstein relation when the growth is studied in liquid:

$$D = \frac{RT}{6\pi N_a \eta a} \quad (4)$$

with N_a the Avogadro's constant, η the viscosity of water, and a the hydrodynamic radius of the solvated ion or molecule. By replacing D in equation (3), the growth constant K can be expressed as:

$$K = \frac{4\gamma V_m^2 C_\infty}{27\pi N_a \eta a} \quad (5)$$

As T does not appear in this expression of the growth rate constant, the temperature dependence of K measured experimentally can be exploited to quantify the variation of C_∞ with temperature. As γ and V_m are not expected to vary in this temperature range, ^[15] the speed-up of the growth processes can be related to the variation of η and C_∞ . The viscosity of water is reduced by 1.6 when the temperature increases from 25 °C to 50 °C and by 2.7 from 25 °C to 85 °C.^[16] Given the higher variability of K with temperature, we can then deduce that C_∞ increases by 2.2 from 25 °C to 50 °C and by 22.6 from 25 °C to 85 °C. From this result, we can quantitatively reconsider the effect of temperature on the nucleation processes. Figure 3b shows the effects of the resulting decrease of S at 50 °C and 85 °C on the nucleation rate. The curves calculated at 25 °C and 50 °C are now nearly confounded which explain the very similar averaged and instantaneous nucleation rates measured experimentally. At 85 °C, the nucleation rate drops much more rapidly when S decreases than at 25 °C and 50 °C which explains the very short nucleation period observed by LCTEM at this temperature. This agreement between experimental observations and classical theories of nucleation and growth reveals that the variation of C_∞ governs the nucleation dynamics when temperature rises.

It is worth discussing the other physicochemical phenomena that could also influence the nucleation and growth processes. At first, thermal effects on the surface chemistry of SiN membranes could impact the dynamics of the heterogeneous nucleation processes observed by LCTEM. Indeed, Wang *et al* have shown that local hydrophilic patches with enhanced concentrations of silanol and silamine groups could reduce the free energy barrier to nucleation.^[17] Therefore, the effect of temperature on the density of these preferential nucleation sites could possibly influence nucleation dynamics, but to our knowledge, such thermal effects have not been reported. The temperature dependence of radiolysis reactions could also play a role in the present experiments. According to the kinetic model proposed by Ambrozic *et al.* the reduction of gold

precursors driven by water radiolysis is slightly favored when the temperature rises from 20 to 60 °C if the pressure inside the liquid-cell is way above atmospheric pressure.^[8a] However, this effect is likely negligible in our experiments, because the low dose rate conditions and the constant liquid flow reduce the formation of gas bubbles that increase the pressure inside the liquid cell. Also, the thermal degradation of chloroauric acid that starts at 75 °C may also influence the reaction kinetics of our experiments performed at 85 °C.^[18]

2.2 Growth mechanisms: seeing beyond the LSW theory

The main interest of our *in situ* TEM approach is to directly observe the impact of temperature on the many scenarios that have been proposed to explain the size and shape of metal colloids and to reveal unexpected atomic-scale mechanisms. As the behavior of NP assemblies is in good agreement with the LSW theory, Ostwald ripening is also expected to contribute to the growth processes. Of course, the different growth kinetics of NPs and the resulting size dispersion of the assemblies suggest the presence of metal transfer between the NPs at any temperature. However, the dissolution of some NPs while other keep growing was only observed at 85 °C (**Figure 4 and S3**) which emphasizes that Ostwald ripening is a thermo-activated process directly related to the solubility of NPs in solution. The fact that NPs with size way above the detection limit dissolve only at high temperature demonstrates once again the increase of NP solubility with temperature. Furthermore, small NPs are expected to be more soluble leading to the idealistic view of Ostwald ripening: the growth of larger NPs at the expense of the small ones. However, as illustrated in figure 4 and S3, both small and large NPs can shrink and disappear in the liquid-cell at high temperature. On several videos, we measured the size of NPs on the last image before shrinking processes are detected. We found mean sizes of 38 nm and 57 nm for the NPs that shrink and grow, respectively which shows that on average small NPs are more prone to dissolve. However, 20% of the NPs that

dissolved had a size above 57 nm before shrinking. These *in situ* observations highlight that size is not the only parameter ruling the Ostwald ripening mechanisms and question this basic assumption of the LSW theory. By relying on liquid phase TEM studies of individual nano-objects dissolution^[19] and the selective etching strategies used in colloidal chemistry to select the shape of metal nano-seeds,^[20] we can reasonably assume that the surface structure of NPs and the presence of defects also impact the degradability of gold NPs.

Coalescence phenomena are also observed when neighboring nanocrystals get in contact. As the NPs are motionless on the SiN membranes, the much higher density of NPs formed at 25 °C greatly favors their coalescence leading to a clear reduction of N (Figure 2a) and a slight increase of the growth rate once the nucleation phase is over (Figure 2c). As already reported,^[1b, 10b] this growth mechanism induces a broader and more symmetrical size distribution than the one expected in the LSW theory (**Figure S4a**). The size distribution of NPs formed at 50 °C (Figure S4b) where no coalescence is observed, is more in agreement with the prediction of the LSW theory with the characteristic asymmetry at the higher particle diameter side cutting off sharply when the radius is 1.4 times the average radius.

2.3 Temperature effects on the shape of nanocrystals: When the competition between the deposition and the surface diffusion of atoms dictates the faceting processes.

Surface diffusion plays a major role in the growth pathway of nanomaterials. Xia and co-workers have demonstrated that the final shape of noble-metal NPs synthesized in solution can be finely controlled by tuning the ratio between the rates for atom deposition and surface diffusion ($V_{\text{deposition}}/V_{\text{diffusion}}$).^[1c] Of course, these two atomic-scale processes speed up when increasing temperature, but the radiolysis-driven synthesis performed by LCTEM offers the opportunity to tune the $V_{\text{deposition}}/V_{\text{diffusion}}$ with the electron dose rate that allows controlling the reaction kinetics

and the deposition speed without influencing the diffusion processes. As seen in Figure 1 and S1, in low \dot{d} conditions faceted NPs are formed at low and high temperature, because the deposition rate is slow enough to give the nanostructures the time needed to reconstruct thermodynamically stable surfaces. In these low $V_{\text{deposition}}/V_{\text{diffusion}}$ conditions, the shape of nanocrystals is then driven by crystal defect formation leading to icosahedral, decahedral or 2D nanostructures that mainly exhibit $\{111\}$ facets.^[6c, 21] However, the shape of NPs obtained at higher \dot{d} drastically changes with temperature. At 25 °C, multigrain dendritic morphologies are formed when the dose rate exceed 30 electrons.nm⁻².s⁻¹ (**Figure 5a and S5a**). These polycrystalline structures with very rough surfaces that most likely present high index facets result from a high $V_{\text{deposition}}/V_{\text{diffusion}}$ ratio, because the slow surface diffusion at this temperature cannot counterbalance the fast deposition and merging processes driven by high \dot{d} radiolysis. On the contrary, well faceted NPs are obtained at 85 °C even when the dose rate largely exceed 30 electrons.nm⁻².s⁻¹ (Figure 5b, 5c and S5b). These results illustrate that increasing the temperature of the reaction media allows maintaining the growth under thermodynamic control over a much larger range of deposition rate. It is worth noting that the nanocrystal shapes obtained in this intermediate $V_{\text{deposition}}/V_{\text{diffusion}}$ regime differ from the one obtained at low $V_{\text{deposition}}/V_{\text{diffusion}}$ ratio, with in particular the presence of many nanocubes and nanorods (Figure 5b, 5c and S5b) that were never observed at low \dot{d} (Figure 1). The formation of nanocubes with mainly $\{100\}$ facets is in line with the bench-scale syntheses of Xia et al. in which Pd nanocubes were obtained with intermediate $V_{\text{deposition}}/V_{\text{diffusion}}$ ratio, while nanostructures with high index facets and $\{111\}$ facets were obtained with high and low $V_{\text{deposition}}/V_{\text{diffusion}}$ ratios, respectively.^[1c] The variability of nanocrystal shape in the assemblies formed at high temperature is also dictated by crystal defect dynamics at the early stage of the growth, because our *in situ* synthesis protocol does not rely on seed-mediated synthesis.

3. Conclusion

We exploited temperature-controlled LCTEM to study thermal effects on the formation mechanisms of gold NPs from the colloidal assembly scale down to the single NP level. By quantitatively comparing our real time *in situ* observations with classical models for NP nucleation and growth, we showed that the temperature-induced changes in the collective behavior of NPs are explained by the increase of molecular diffusion and NP solubility with temperature. Besides, monitoring the dynamics of individual NPs provides a better understanding of Ostwald ripening that turns out to be driven not only by size effects but also by crystal defects. Finally, by controlling the reaction kinetics with both the temperature and the electron dose rate, we evidenced how the competition between atom deposition and surface diffusion rules the final shape of nanostructures. As the present methodology can easily be applied to other chemical reactions at the interface between solids and liquids, this work illustrates the extended potential of temperature-controlled LCTEM to visualize thermal effects in nanochemistry and to image nanoscale processes that only occur in hot liquid.

4. Experimental section

The experimental protocol used in this paper was described in details in a recent methodological paper.^[12] Briefly, the sample solution is composed of 1 mM of gold(III) chloride trihydrate (HAuCl₄) purchased from Sigma Aldrich Inc. diluted in Milli-Q water. We used heating liquid-cells commercialized by Protochips Inc. They consist of two silicon wafers with dimensions of 2 * 2 mm and 4.5 * 6 mm, called the small and large E-chips respectively. Each E-chip has one 550 μm * 50 μm observation window covered by a 50 nm thick Si₃N₄ amorphous film. The small E-chips have 150 nm gold spacers that fixe the distance between the two E-chips and the large one

present an embedded resistance that allows a uniform heating of the liquid sample. Both E-chips were cleaned using a Gatan plasma cleaner to make them hydrophilic. Before assembling the liquid-cell, we put a droplet of 2 μL of the HAuCl_4 solution on the small E-chip. The large E-chip was then placed over the small one with their windows in cross-configuration, giving a square field of view of 50 μm edge length. We performed the experiments in the corner of the SiN window in order to minimize the liquid thickness. Previous EFTEM measurements demonstrated that the liquid thickness in this area of the liquid cell varies from 250 to 600 nm.^[22] We used the liquid cell holder with heating and flow capability commercialized by Protochips Inc. All the low-magnification STEM data (Figure 1) were obtained using a JEOL 2100 Plus electron microscope operating at 200 kV with a beam current of 24 pA. All the high-magnification STEM data (Figure 4, 5 S3 and S5) were obtained using a JEOL ARM 200 F electron microscope operating at 200 kV with a beam current ranging from 3 to 18 pA. The electron dose rate was calculated by dividing the beam current by the surface of STEM images. The solution of gold precursors was continuously injected inside the liquid-cell during the experiment at a rate of $5\mu\text{L}\cdot\text{min}^{-1}$. In spite of this use of the liquid cell in flow mode, it is worth noting that the nucleation and growth dynamics tend to slow down after recording several videos in a liquid cell. As already described in previous reports,^[23] this effect is due to the decrease of the gold-precursor concentration in the liquid cell when repeating several NP growth experiments. To overcome this issue, the data shown in this paper were all acquired in the first 15 minutes of use of the liquid-cells.

Unlike our previous methodological paper,^[12] STEM videos were digitally processed and analyzed using the free PlugIM platform developed by IFPEN. Here is the list of the plugins used for extracting quantitative information from the STEM video data: Edge preserving filter, Luminosity drift correction, Histogram segmentation, Border kill, Criterion opening, Hole filling and Binary separation.

Supporting Information

Supporting Information is available from the Wiley Online Library or from the author.

Acknowledgments

We gratefully acknowledge the help of Maxime Moreaud in the processing of our videos using the PlugIM platform developed at IFPEN. We also acknowledge the financial support of the Region Ile-de-France (convention SESAME E1845 for the JEOL ARM 200F electron microscope installed at the University of Paris), the Labex SEAM and the CNRS.

Received: ((will be filled in by the editorial staff))

Revised: ((will be filled in by the editorial staff))

Published online: ((will be filled in by the editorial staff))

References

- [1] a) N. T. Thanh, N. Maclean, S. Mahiddine, *Chem. Rev.* **2014**, 114, 7610; b) R. Viswanatha, D. D. Sarma, in *Nanomaterials chemistry: recent developments and new directions*, (Eds: C. Rao, A. Müller, A. Cheetham), Wiley-VCH Verlag GmbH & Co. KGaA, Weinheim 2007, 139; c) X. Xia, S. Xie, M. Liu, H.-C. Peng, N. Lu, J. Wang, M. J. Kim, Y. Xia, *Proceedings of the National Academy of Sciences* **2013**, 110, 6669.
- [2] a) J. E. Millstone, S. J. Hurst, G. S. Métraux, J. I. Cutler, C. A. Mirkin, *small* **2009**, 5, 646; b) Y. Xia, Y. Xiong, B. Lim, S. E. Skrabalak, *Angew. Chem. Int. Ed.* **2009**, 48, 60; c) H. Dong, Y. C. Chen, C. Feldmann, *Green Chemistry* **2015**, 17, 4107.
- [3] a) R. Seshadri, G. N. Subbanna, V. Vijayakrishnan, G. U. Kulkarni, G. Ananthakrishna, C. N. R. Rao, *The Journal of Physical Chemistry* **1995**, 99, 5639; b) G. Oskam, A. Nellore, R. L. Penn, P. C. Searson, *The Journal of Physical Chemistry B* **2003**, 107, 1734; c) Z. Hu, D. J. Escamilla Ramirez, B. E. Heredia Cervera, G. Oskam, P. C. Searson, *The Journal of Physical Chemistry B* **2005**, 109, 11209; d) B. Abécassis, F. Testard, O. Spalla, P. Barboux, *Nano Lett.* **2007**, 7, 1723; e) R. Viswanatha, P. K. Santra, C. Dasgupta, D. D. Sarma, *Phys. Rev. Lett.* **2007**, 98, 255501; f) K. Biswas, N. Varghese, C. N. R. Rao, *Small* **2008**, 4, 649; g) B. Abécassis, F. Testard, Q. Kong, B. Francois, O. Spalla, *Langmuir* **2010**, 26, 13847; h) J. G. Parsons, V. Armendariz, M. L. Lopez, M. Jose-Yacaman, J. L. Gardea-Torresdey, *J. Nanopart. Res.* **2010**, 12, 1579; i) Y. Zhou, H. Wang, W. Lin, L. Lin, Y. Gao, F. Yang, M. Du, W. Fang, J. Huang, D. Sun, Q. Li, *J. Colloid Interface Sci.* **2013**, 407, 8; j) J. Polte, T. T. Ahner, F. Delissen, S. Sokolov, F. Emmerling, A. F. Thünemann, R. Kraehnert, *J. Am. Chem. Soc.* **2010**, 132, 1296.
- [4] a) V. K. LaMer, R. H. Dinagar, *J. Am. Chem. Soc.* **1950**, 72, 4847; b) I. M. Lifshitz, V. V. Slyozov, *J. Phys. Chem. Solids* **1961**, 19, 35; c) C. Wagner, *Zeitschrift für Elektrochemie, Berichte der Bunsengesellschaft für physikalische Chemie* **1961**, 65, 581.
- [5] a) T. Ngo, H. Yang, *The Journal of Physical Chemistry Letters* **2015**, 6, 5051; b) F. M. Ross, *Science* **2015**, 350, 1490; c) H. G. Liao, K. Y. Niu, H. M. Zheng, *Chem. Commun.* **2013**, 49, 11720.

- [6] a) T. J. Woehl, *Chem. Mater.* **2020**, 32, 7569; b) A. V. Ievlev, S. Jesse, T. J. Cochell, R. R. Unocic, V. A. Protopopescu, S. V. Kalinin, *ACS Nano* **2015**, 9, 11784; c) D. Alloyeau, W. Dachraoui, Y. Javed, H. Belkahla, G. Wang, H. Lecoq, S. Ammar, O. Ersen, A. Wisnet, F. Gazeau, C. Ricolleau, *Nano Letters* **2015**, 15, 2574.
- [7] a) H.-G. Liao, D. Zherebetsky, H. Xin, C. Czarnik, P. Ercius, H. Elmlund, M. Pan, L.-W. Wang, H. Zheng, *Science* **2014**, 345, 916; b) N. Ahmad, Y. Le Bouar, C. Ricolleau, D. Alloyeau, *Adv. Struct. and Chem. Im.* **2016**, 2, 9; c) N. Ahmad, G. Wang, J. Nelayah, C. Ricolleau, D. Alloyeau, *Nano Letters* **2017**, 17, 4194; d) K. Aliyah, J. Lyu, C. Goldmann, T. Bizien, C. Hamon, D. Alloyeau, D. Constantin, *The Journal of Physical Chemistry Letters* **2020**, 11, 2830.
- [8] a) B. Ambrožič, A. Prašnikar, N. Hodnik, N. Kostevšek, B. Likozar, K. Ž. Rožman, S. Šturm, *Chemical Science* **2019**, 10, 8735; b) S. F. Tan, G. Bisht, U. Anand, M. Bosman, X. E. Yong, U. Mirsaidov, *J. Am. Chem. Soc.* **2018**, 140, 11680; c) J. Lyu, X. Gong, S.-J. Lee, K. Gnanasekaran, X. Zhang, M. C. Wasson, X. Wang, P. Bai, X. Guo, N. C. Gianneschi, O. K. Farha, *J. Am. Chem. Soc.* **2020**, 142, 4609; d) J. T. van Omme, H. Wu, H. Sun, A. F. Beker, M. Lemang, R. G. Spruit, S. P. Maddala, A. Rakowski, H. Friedrich, J. P. Patterson, *Journal of Materials Chemistry C* **2020**, 8, 10781.
- [9] N. M. Schneider, M. M. Norton, B. J. Mendel, J. M. Grogan, F. M. Ross, H. H. Bau, *J. Phys. Chem. C* **2014**, 118, 22373.
- [10] a) T. J. Woehl, J. E. Evans, I. Arslan, W. D. Ristenpart, N. D. Browning, *ACS Nano* **2012**, 6, 8599; b) T. J. Woehl, C. Park, J. E. Evans, I. Arslan, W. D. Ristenpart, N. D. Browning, *Nano Letters* **2014**, 14, 373.
- [11] W.-G. Jung, J. H. Park, Y.-R. Jo, B.-J. Kim, *Journal of the American Chemical Society* **2019**, 141, 12601.
- [12] A. Khelfa, J. Nelayah, G. Wang, C. Ricolleau, D. Alloyeau, *JoVE* **2021**, e62225.
- [13] A. Zangwill, *Physics at surfaces*, Cambridge university press, **1988**.
- [14] J. A. Powell, R. M. Schwieters, K. W. Bayliff, E. N. Herman, N. J. Hotvedt, J. R. Changstrom, A. Chakrabarti, C. M. Sorensen, *RSC Advances* **2016**, 6, 70638.
- [15] a) S. Ali, V. Myasnichenko, E. Neyts, *Physical Chemistry Chemical Physics* **2016**, 18, 792; b) M. G. Pamato, I. G. Wood, D. P. Dobson, S. A. Hunt, L. Vočadlo, *Journal of applied crystallography* **2018**, 51, 470.
- [16] L. Korson, W. Drost-Hansen, F. J. Millero, *The Journal of Physical Chemistry* **1969**, 73, 34.
- [17] M. Wang, T. U. Dissanayake, C. Park, K. Gaskell, T. J. Woehl, *J. Am. Chem. Soc.* **2019**, 141, 13516.
- [18] K. Otto, I. Oja Acik, M. Krunks, K. Tõnsuaadu, A. Mere, *Journal of Thermal Analysis and Calorimetry* **2014**, 118, 1065.
- [19] a) M. J. Meijerink, K. P. de Jong, J. Zečević, *The Journal of Physical Chemistry C* **2020**, 124, 2202; b) J. Wu, W. Gao, H. Yang, J.-M. Zuo, *ACS nano* **2017**, 11, 1696; c) A. Khelfa, J. Meng, C. Byun, G. Wang, J. Nelayah, C. Ricolleau, H. Amara, H. Guesmi, D. Alloyeau, *Nanoscale* **2020**, 12, 22658.
- [20] Y. Zheng, J. Zeng, A. Ruditskiy, M. Liu, Y. Xia, *Chemistry of Materials* **2014**, 26, 22.
- [21] C. Lofton, W. Sigmund, *Adv. Funct. Mater.* **2005**, 15, 1197.
- [22] M. Piffoux, N. Ahmad, J. Nelayah, C. Wilhelm, A. Silva, F. Gazeau, D. Alloyeau, *Nanoscale* **2017**, 10, 1234.
- [23] P. Abellan, T. J. Woehl, L. R. Parent, N. D. Browning, J. E. Evans, I. Arslan, *Chem. Commun.* **2014**, 50, 4873.

Figures:

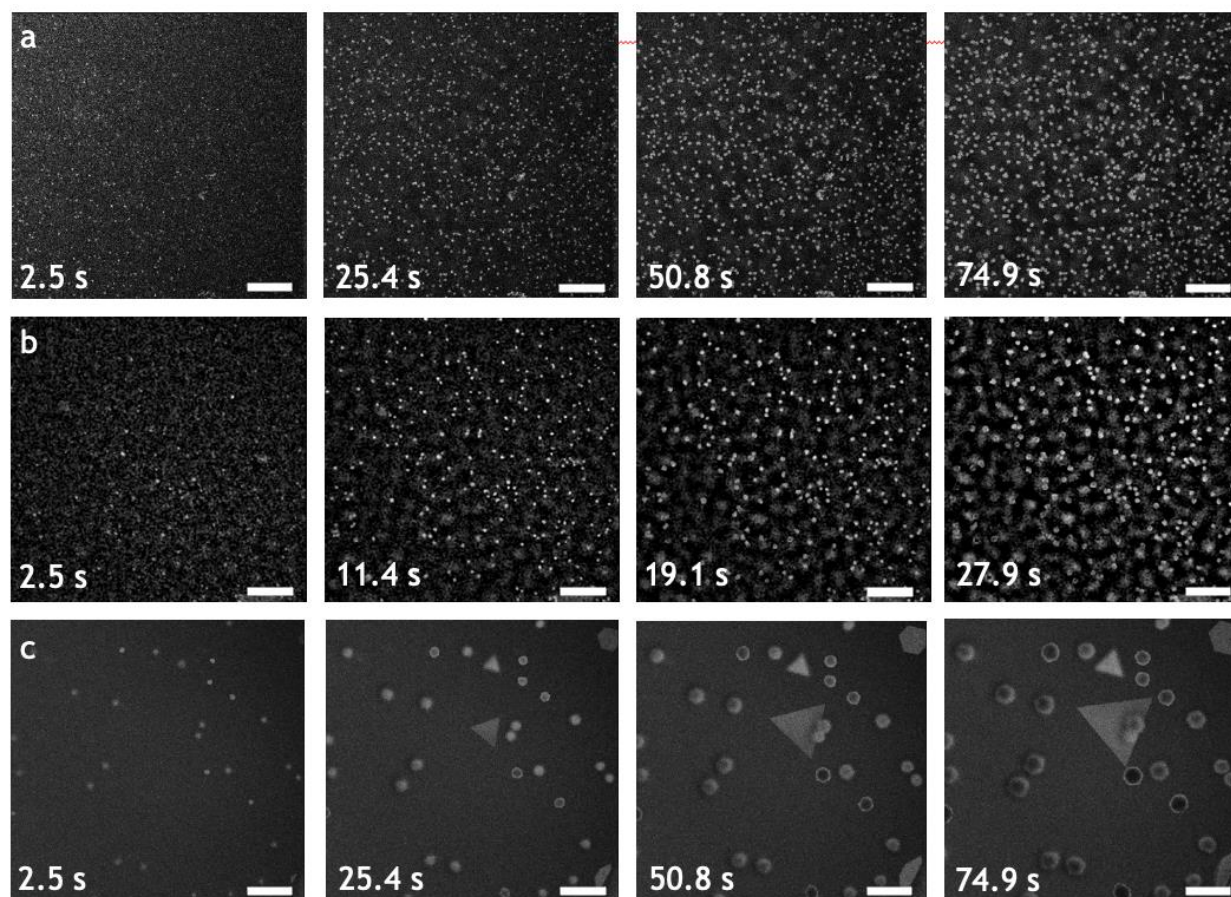


Figure 1. Low magnification STEM HAADF image series of the radiolysis-driven formation of gold NPs in water at (a) 25 °C, (b) 50 °C and (c) 85 °C. The acquisition time is indicated in the bottom left corner of each image. All scale bars correspond to 1 μm . The three image series were acquired with a continuous electron dose rate of $3.4 \text{ electrons}\cdot\text{nm}^{-2}\cdot\text{s}^{-1}$.

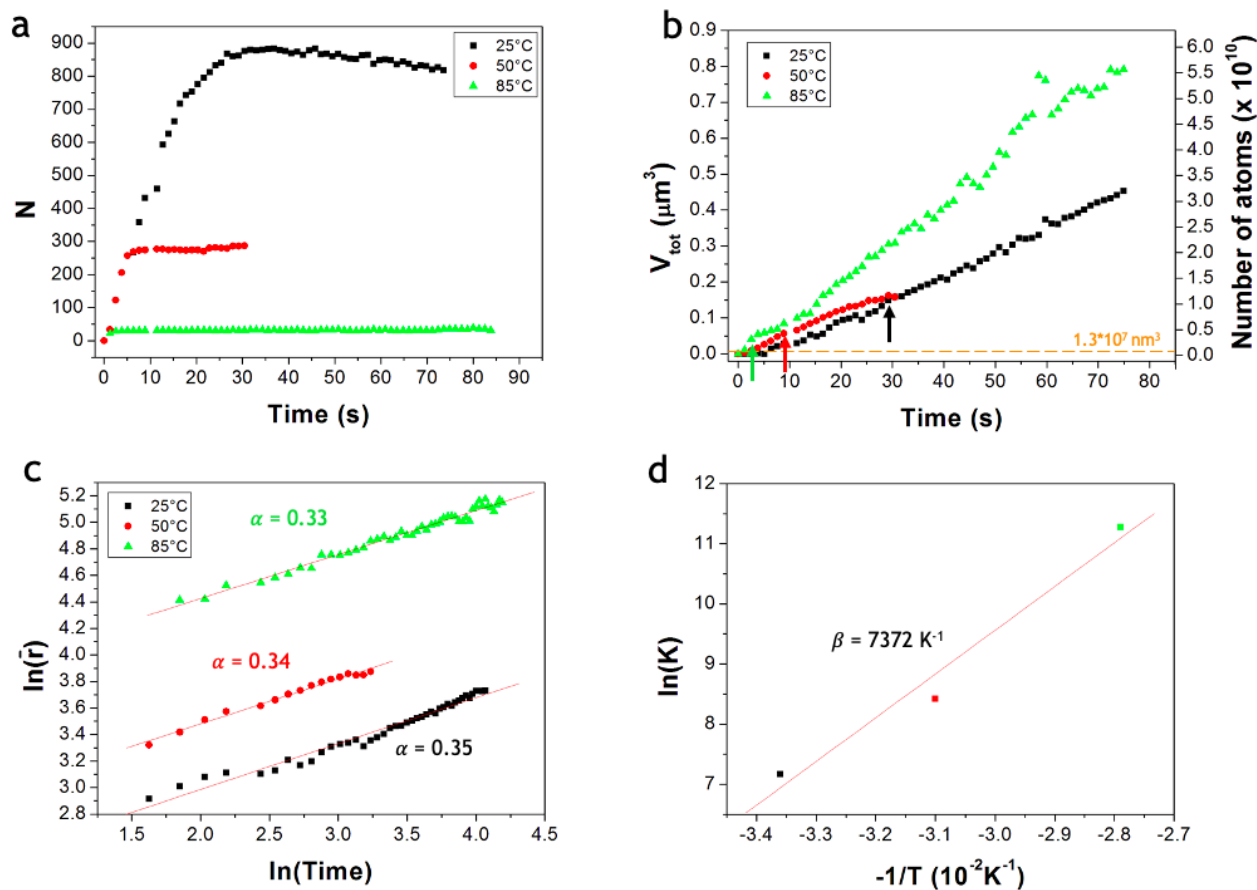


Figure 2. Graphs quantifying the nucleation and growth of gold NPs at 25 °C (black), 50 °C (red) and 85 °C (green). (a) Number of NPs (N) as a function of time. (b) Total volume of gold NPs (V_{tot}) in μm^3 (left axis) and in number of gold atoms (right axis) as a function of time. The orange line represents the number of molecules of HAuCl_4 in the observation area before irradiation calculated with an average liquid thickness of 500 nm. (c) Logarithm of the average radius (\bar{r}) of NPs as a function of the logarithm of time. The slope of the linear fit (α) is indicated for each temperature. (d) Logarithm of the growth rate constant (K) as a function of the $-1/T$ (β corresponds to the slope of the linear fit of the data).

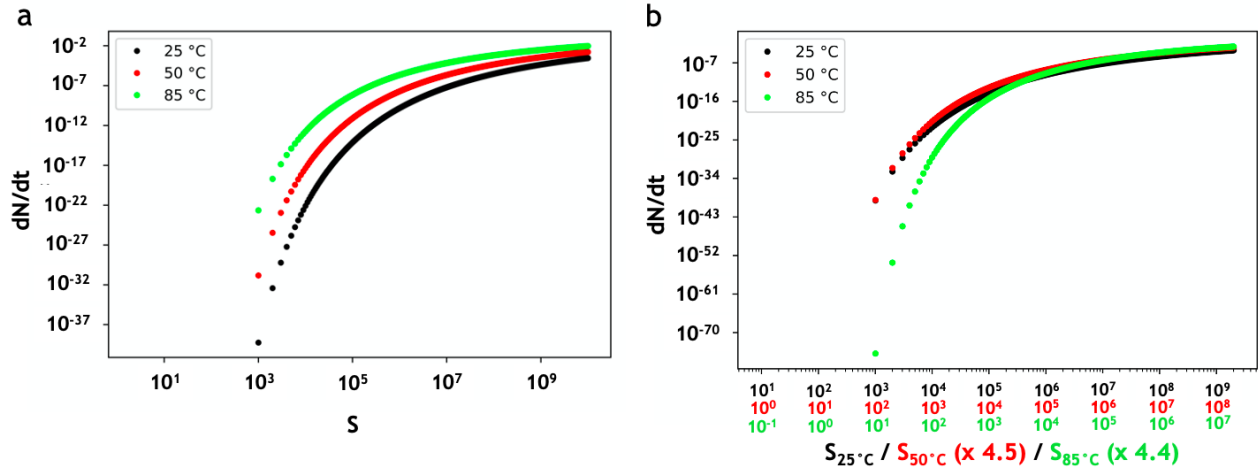


Figure 3. Nucleation rate (dN/dt) calculated using equation (1) with $\phi = 0.5$ and $\gamma = 0.5 \text{ J} \cdot \text{m}^{-2}$, as a function of the supersaturation ratio (S) in log-log scale. (b) Nucleation rate calculated using equation (1) with $\phi = 0.5$ and $\gamma = 0.5 \text{ J} \cdot \text{m}^{-2}$ as a function of the supersaturation ratio in log-log scale. These calculations take into account the experimentally deduced increase of C_∞ with temperature: $C_\infty^{50^\circ\text{C}} = 2.2 \times C_\infty^{25^\circ\text{C}}$ and $C_\infty^{85^\circ\text{C}} = 22.6 \times C_\infty^{25^\circ\text{C}}$. As $S = C_{\text{Au}}/C_\infty$, the corresponding S is indicated on the x-axis for each temperature (in black: $S_{25^\circ\text{C}}$; in red: $S_{50^\circ\text{C}} = S_{25^\circ\text{C}}/2.2$; in green: $S_{85^\circ\text{C}} = S_{25^\circ\text{C}}/22.6$).

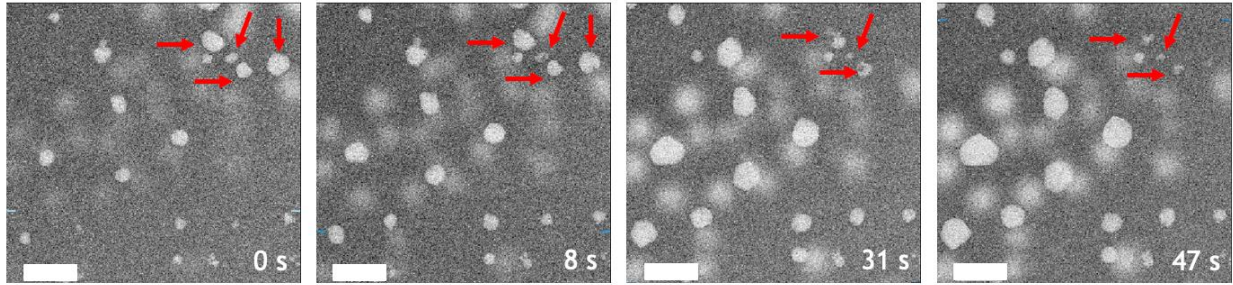


Figure 4. High-magnification STEM HAADF image series at 85 °C showing Ostwald ripening process during the growth of gold NPs. The red arrows indicate the NPs that shrink. The acquisition time is indicated in the bottom right corner of each image. All scale bars correspond to 250 nm. Image series acquired with a continuous electron dose rate of $20.9 \text{ electrons.nm}^{-2}.\text{s}^{-1}$.

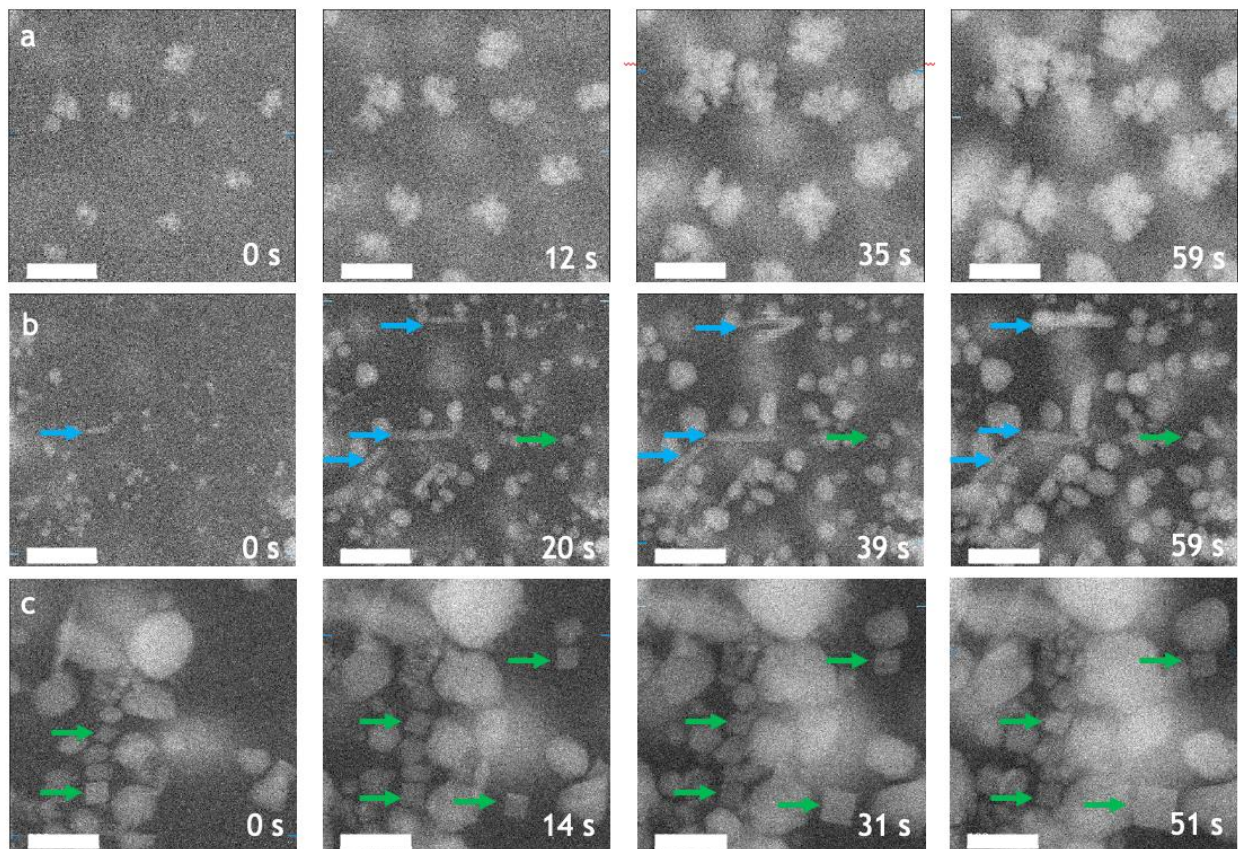


Figure 5. High-magnification STEM HAADF image series of the growth of gold NPs. (a) At 25 °C, dendritic NPs are obtained. (b-c) At 85 °C, faceted NPs are obtained. Nanorods and nanocubes are indicated with blue and green arrows, respectively. (a) and (b) image series were acquired with a continuous electron dose rate of $30.1 \text{ electrons.nm}^{-2}.\text{s}^{-1}$ and the scale bars correspond to 200 nm. The (c) image series was acquired with a continuous electron dose rate of $83.6 \text{ electrons.nm}^{-2}.\text{s}^{-1}$ and the scale bars correspond to 100 nm. The acquisition time is indicated in the bottom right corner of each image.

TOC

We reveal how the temperature affects the formation of gold nanoparticles in water by liquid-phase transmission electron microscopy. Thermal effects on the nucleation and growth rates of colloidal assemblies match with the classical models for nanoparticle formation but the direct observation of single nanoparticle dynamics provides new in situ insights into the atomic-scale mechanisms governing the size and shape of nanostructures.

Graphical TOC

